LTCC Magnetic Sensors at EPFL and TCV: Lessons Learnt for ITER

D.Testa[1], A.Corne[1,2], C.Jacq[2], T.Maeder[2], M.Toussaint[1], S.Antonioni[1], R.Chavan[1], S.Couturier[1], F.Dolizy[1], P.Lavanchy[1], J.B.Lister[1], X.Llobet[1], B.Marletaz[1], P.Marmillod[1], C.Moura[1], U.Siravo[1], M.Stoeck[1,2], L.Blondel[1], B.Ellenrieder[1,2], G.Farine[2], Y.Fournier[2], M.Garcin[2], A.Iantchenko[1,3], L.Perrone[1], L.Stipani[1], A.Tolio[1,4], P.Windischofer[1,5], the EUROfusion MST1 team[a], the TCV team

[1]*Ecole Polytechnique Fédérale de Lausanne (EPFL), Swiss Plasma Center (SPC), CH-1015 Lausanne, Switzerland*
[2]*Ecole Polytechnique Fédérale de Lausanne (EPFL), Laboratoire de Production Microtechnique (LPM), CH-1015 Lausanne, Switzerland*
[3]*formerly at Chalmers University of Technology (Sweden), exchange student with EPFL-SPC, Switzerland*
[4]*formerly at Politecnico di Milano (Italy), exchange student with EPFL-SPC, Switzerland*
[5]*formerly at Technical University of Wien (Austria), exchange student with EPFL-SPC, Switzerland*

Innovative 3D high-frequency magnetic sensors have been designed and manufactured in-house for installation on the Tokamak à Configuration Variable (TCV), and are currently routinely operational. These sensors combine the Low Temperature Co-fired Ceramic (LTCC) and the thick-film technologies, and are in various aspects similar to the majority of the inductive magnetic sensors currently being procured for ITER (290 out of 505 are LTCC-1D). The TCV LTCC-3D magnetic sensors provide measurements in the frequency range up to 1MHz of the perturbations to the toroidal (quasi-parallel: $\delta B_{TOR} \sim \delta B_{PAR}$), vertical (quasi-poloidal: $\delta B_{VER} \sim \delta B_{POL}$), and radial ($\delta B_{RAD}$) magnetic field components, the latter being generally different from the component normal to the Last Closed Flux-Surface (δB_{NOR}). The LTCC-3D δB_{RAD} measurements improve significantly on the corresponding data with the saddle loops, which are mounted onto the wall and have a bandwidth of ~3kHz (due to the wall penetration time). The LTCC-3D δB_{TOR} measurements (not previously available in TCV) provide evidence that certain MHD modes have a finite δB_{PAR} at the LCFS, as recently calculated for pressure-driven instabilities. The LTCC-3D δB_{POL} measurements allow to cross-check the data obtained with the Mirnov coils, and led to the identification of large EM noise pick-up for the Mirnov DAQ. The LTCC-3D data for δB_{POL} agree with those obtained with the Mirnov sensors in the frequency range where the respective data acquisition overlap, routinely up to 125kHz, and up to 250kHz in some discharges, when the EM noise pick-up on the Mirnov DAQ is removed. Finally, we look at what lessons can be learnt from our work for the forthcoming procurement, installation and operation of the LTCC-1D sensors in ITER.
Keywords: magnetic sensors, ITER, TCV, LTCC technology.

1. Introduction

The Low-Temperature Co-fired Ceramic (LTCC) technology is an industry standard widely used in harsh environmental conditions, covering a large spectrum of applications [1]. Magnetic sensors produced using the similar HTCC (high-temperature) technology were first briefly used in LHD and NSTX in the late 90's [2]. The LTCC technology has also being considered for discrete magnetic sensors to be used in ITER since 2007 [3, 4]. Various examples of LTCC magnetic sensors have been designed and manufactured at EPFL during the course of a 10 year project [5-9]. The main achievements at EPFL have been being able to replicate the high manufacturing yields and very high reproducibility obtained in industry at a fraction of the costs for a very small production batch, the cost vs. yields hampering developments in other non-industrial facilities. LTCC-1D sensors designed and built at EPFL were installed on FTU in 2010 (operational, used for fluctuations). LTCC-2D sensors designed and built at EPFL were installed on WEST in 2014 (operational, used for equilibrium/fluctuations in the divertor region). Based on this prototyping work, most of the ITER in-vessel inductive magnetic sensors (290 out of 505 [10, 11]) currently being procured are of the LTCC-1D type.

The TCV LTCC-3D sensors are mounted on the inside of the vacuum wall and, when considering the toroidal coordinate system ($\mathbf{e_\phi}$, $\mathbf{e_Z}$, $\mathbf{e_R}$), provide measurements of the perturbation to the toroidal ($\delta B_{TOR} \| \mathbf{e_\phi}$), vertical ($\delta B_{VER} \| \mathbf{e_Z}$) and radial ($\delta B_{RAD} \| \mathbf{e_R}$) magnetic field components in the frequency range up to 1MHz. Knowledge of the equilibrium topology at the Last Closed Flux Surface (LCFS) allows to transform the geometrical, wall-aligned measurements into the corresponding flux-coordinate ones ($\mathbf{e_\parallel}$, $\mathbf{e_\theta}$, $\mathbf{e_\rho}$), namely the parallel ($\delta B_{PAR} \| \mathbf{e_\parallel}$), poloidal ($\delta B_{POL} \| \mathbf{e_\theta}$) and normal ($\delta B_{NOR} \| \mathbf{e_\rho}$) components.

2. Design principles for the LTCC sensors

The LTCC sensor is built up from thin ceramic tapes (*layers*), on which a metallic ink is screen-printed to form windings (*turns*) and ensure inter-layer connection (*vias*). For multi-D sensors, sets of LTCC-1D modules are then mounted onto an alumina base, which can also be used as a measurement axis. To illustrate the winding pattern, fig1 shows a 3D view of a LTCC-1D magnetic sensor.

The design principles for all our LTCC sensors aim at optimizing the effective area (NA_{EFF}) and self-inductance (L_{SELF}) for the intended frequency range of operation, i.e. low-frequency (equilibrium, <10kHz) or high-frequency (fluctuations) analyses. For multi-D sensors, this is done for each measurement axis, while reducing the mutual (L_{MUT}) and parasitic (NA_{PAR}) coupling between them.

[a] See the author list of *Overview of progress in European Medium Sized Tokamaks towards an integrated plasma-edge/wall solution*, by H.Meyer et al, Nucl. Fusion 57 102014 (2017).

author's email: duccio.testa@epfl.ch

These design principles have to be considered together with the installation constraints, specifying the maximum size of the sensor. Thus the NA_{EFF} vs. L_{SELF} optimization is performed primarily over the number of layers and turns/layer, and on the winding pattern (concentric or racetrack, see fig2). Initial prototyping for the LTCC-1D sensors was also performed by varying the width and thickness of the windings and the separation between them, using different winding patterns on consecutive layers with normal or recto-verso printing, but lately all these parameters have been kept practically fixed to simplify the manufacturing as their impact is relatively small on NA_{EFF} and L_{SELF}. All this prototyping work has been used for the development of the actual ITER LTCC-1D sensors. Additionally, for multi-D sensors particular attention has to be paid to the on-board wiring connecting the different sets of LTCC-1D modules, as this has, on the other hand, a significant impact on NA_{PAR} and L_{MUT}.

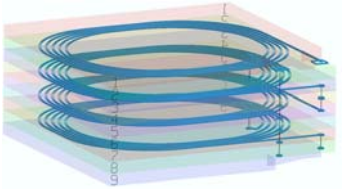

Fig1. A 3D view of a LTCC-1D sensor, to illustrate the winding pattern and the inter-layer connection though the vias.

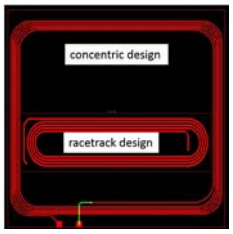

Fig2. Concentric vs. racetrack design for the winding in one layer.

The physics requirements for our latest LTCC-3D sensors are set by the installation of two high-power, high-energy NBI systems on TCV [12], namely studying fast ions physics, coherent instabilities and turbulence in the Alfvén frequency range >100kHz and up to 1MHz.

More details on the design principles and design steps, manufacturing processes and physics requirements for our LTCC sensors can be found in [3-10, 13].

3. Installation of the LTCC-3D sensors in TCV

Three LTCC-3D sensors have been installed in TCV, at different toroidal locations identified by their sector number: {02B, 14B, 16A}. In-vessel installation of the sensor+cabling assembly is performed during a manual entry in TCV: the assembly is fixed to a pre-existing rail, and the in-vessel cables are then guided through attachments to other rails to the in-vessel side of the multi-pole vacuum feedthrough used in TCV. Connection of the in-vessel and ex-vessel cables to the feedthrough is also a very complex operation, where a female connector is soldered onto the ex-vessel male end of a molybdenum pin. Particular attention was devoted to optimizing the in-vessel and ex-vessel cabling, reducing as much as possible its overall length and choosing cables with the lower capacitance/meter, to maintain the largest possible bandwidth. Figure3 shows one LTCC-3D sensor as installed in-vessel behind the protection tiles, sitting just above one Mirnov sensor. Note the metal holder used for attachment to the rail and the in-vessel cables brazed onto the sensor's output connection pins.

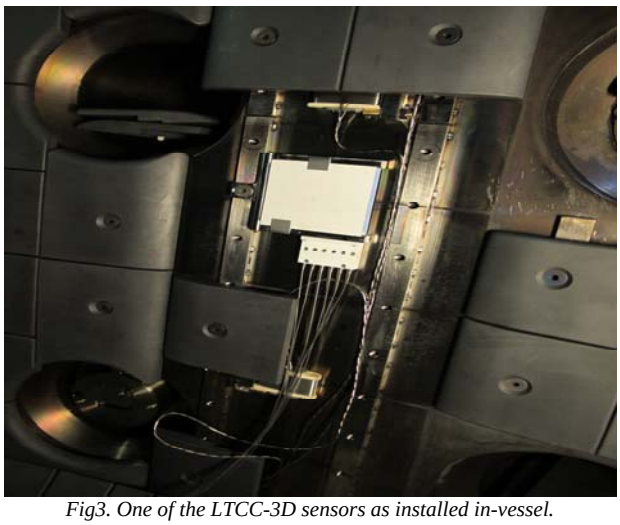

Fig3. One of the LTCC-3D sensors as installed in-vessel.

4. End-to-end system commissioning

The end-to-end system commissioning takes places in different phases, essentially separating the in-vessel and ex-vessel components up to the input of the front-end electronics, and then the remaining ex-vessel components up to the data as stored in the MDS repository. Different transfer functions are obtained for all these elements, which are then combined into the overall calibration steps.

For the first set of components (the sensor, in-vessel cabling, the feedthrough and ex-vessel cabling up to the input of the front-end electronics), we use an Helmholtz coil assembly in the range 10Hz→50kHz to measure the frequency-dependent $NA_{EFF}(\omega)$ and $NA_{PAR}(\omega)$, and then extrapolate the fit to the measurements up to 1MHz. The extrapolation uses the analytical rational function best-fit to the measurements of the effective and parasitic areas, and it is constrained by the errors on the measurements. More details on this procedure will be provided in [13]. An impedance meter is then used in the frequency range 10Hz→13MHz to measure the line impedance, and deduce the corresponding transfer function $H_1(\omega)$. For the second set of components, which includes all the elements of the DAQ up to the data stored in the MDS repository, a function generator is used to give a voltage input during a frequency sweep in the range 10Hz→5MHz. A synchronized reference signal, which does not pass through the DAQ but goes directly to the data repository, is collected with the output voltage from the DAQ, the ratio of the two giving the second transfer function $H_2(\omega)$. Thus we have in Fourier space:

$$\begin{aligned} V_{MEAS}(\omega) &= V_{PROBE}(\omega) H_1(\omega) H_2(\omega) \\ &= \left[i\omega \times H_1(\omega) H_2(\omega) NA_{EFF}(\omega) \right] \times \delta B_{MEAS}(\omega) \end{aligned} \quad (1)$$

The numerical methods associated with the extraction of a rational function H in the Laplace s-space and the digital z-domain from the actual measurements obtained in these different frequency ranges, are described in [8]. The sampling frequency for the LTCC-3D sensors during TCV discharges is 2MHz: thus we use the calibration data beyond 1MHz (not shown here) to estimate correctly the system's end-to-end transfer function and bandwidth.

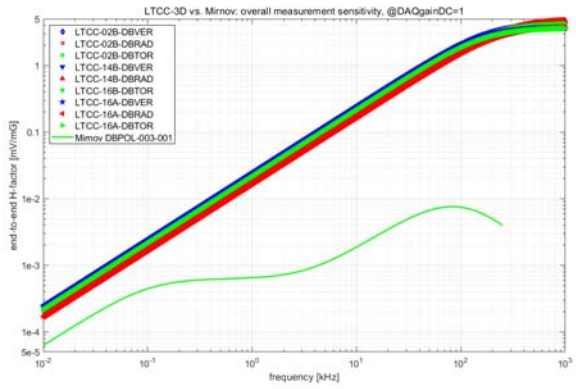

Fig4. Comparing the overall measurement sensitivity $H(\omega)=H_1(\omega)H_2(\omega)\times\omega NA_{EFF}(\omega)=V_{MEAS}(\omega)/\delta B(\omega)$ for all the LTCC-3D and one representative Mirnov sensors installed on TCV. Note that the DAQ DC gain is 4 for the LTCC-3D and 32 for the Mirnov sensors.

An insightful representation for the end-to-end TF is obtained when considering all the elements appearing in the square bracket in eq.(1), namely the overall sensitivity $H(\omega)=\omega\times H_1(\omega)H_2(\omega)NA_{EFF}(\omega)$ for the nominal gain=1 in the DAQ. This H-factor has physical units [mV/mG], and its departure from a linear scaling $H(\omega)\propto\omega$ indicates the (in)ability of the system in measuring certain frequency components in the fluctuating $\delta B(\omega)$ spectrum.

Figure4 compares the H-factor for all the installed LTCC-3D and one representative Mirnov sensors. For the LTCC-3D data the linear scaling $H(\omega)\propto\omega$ is the dominant factor, with a moderate flattening from ~200kHz onwards due to a smaller-than-linear frequency dependence of $NA_{EFF}(\omega)\propto 1/|1+(i\omega/\omega_1)|^{1/2}$, due to the distributed nature of the sensor. Conversely, for the Mirnov sensors $H(\omega)$ shows a very clear rollover at ~90kHz, due to the classical frequency dependence linked to capacitive and inductive coupling between the core and the screen of the sensors' wire, $NA_{EFF}(\omega)\propto 1/(1+(i\omega/\omega_1))/(1+(i\omega/\omega_2))$ [14]. The larger $H(\omega)$ for the LTCC-3D sensors only partially comes from the larger DC value of NA_{EFF} (~2x for δB_{VER} and δB_{TOR} and ~3x for δB_{RAD}), but is essentially due to the different setup of the DAQ, which for the Mirnov sensors is mostly common with the acquisition for the equilibrium analysis.

For the LTCC-3D sensors, fig4 shows that our efforts for increasing the measurement bandwidth to as close as possible to 1MHz have been successful, namely we only have a relatively moderate flattening, but no reduction, in $H(\omega)$ with respect to the linear scaling $H(\omega)\propto\omega$ for frequencies >200kHz and up to the MHz range.

5. Illustrative results with the LTCC-3D sensors

As an illustration of the results obtained with the LTCC-3D sensors, we show in fig5 the measurements obtained for the *sawbone* instability [15, 16]. This mode, with features rather similar to the classic fishbones, occurs only for quasi-tangential NB heating (NBH) and, contrary to the fishbone, invariably acts as the sawtooth precursor, hence its name. In the TCV discharge presented here, the sawbone is a dominant m/n=1/1 (with sideband m/n=2/2 and m/n=4/2 components) bursting instability appearing in the frequency range 25→30kHz (due to a large toroidal Doppler shift at the mode location of ~23kHz) of ~1msec duration occurring every 7→10msec, and appearing only during the NBH time window (from 1.70sec to 1.90sec).

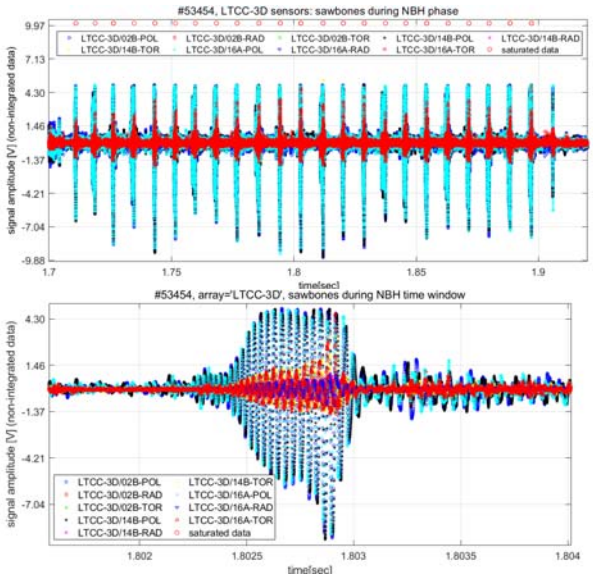

Fig5. The sawbone instability observed with the LTCC-3D sensors in one TCV discharge with NBH. Top frame: all the individual bursts observed during the NBH period. Bottom frame: a zoom of one large burst, showing the relative amplitude of the different δB components.

This mode is observed on all three components of δB, which for the first time provides evidence of a finite δB_{PAR} at the LCFS, validating recent theoretical developments for pressure-driven MHD modes [17]. Also, the δB_{RAD} component of this mode is clearly seen with the LTCC-3D sensors but is completely missed with the saddle loops due to their bandwidth being ~3kHz.

Finally, the LTCC-3D δB_{POL} measurements allow to cross-check the data obtained with the standard Mirnov coils, as there are six Mirnov at the same poloidal position (but in different toroidal sectors) of the three LTCC-3D. Thus, for one largely dominant toroidal mode number and unless toroidal asymmetry is invoked, the data should be very similar, namely all within the uncertainties on the measurement. This comparison is shown in fig6 for some representative frequency ranges in which modes are observed on TCV, and has led to the identification of a large EM noise pick-up for the Mirnov DAQ. To estimate this EM noise, measurements were taken during dedicated (and repeated for statistics) TCV discharges without plasma with the power supplies from the different systems that we believe could introduce EM noise in the {Mirnov, LTCC-3D} systems were individually activated during separate time windows. A Fourier decomposition was then performed, which allows to determine the frequency spectrum of the EM noise, and a frequency-dependent correction can then be implemented. More details on this procedure will be provided in [13]. When this EM noise is correctly accounted for (currently needing a rather cumbersome procedure), we find that the Mirnov and LTCC-3D measurements of δB_{POL} are overall in good agreement, within the expected 20% relative uncertainty.

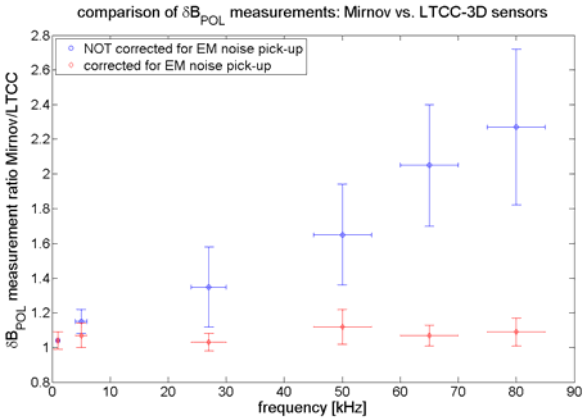

Fig6. Comparison between the LTCC-3D and the Mirnov δB_{POL} measurements. The horizontal error bars represent the frequency range where the main modes are found on TCV, typically tearing modes at ~1kHz and ~5kHz, sawbones at ~27kHz, energetic-particle driven geodesic acoustic modes and global Alfvén Eigenmodes from ~45kHz to ~90kHz. The vertical error bars represent the scatter over the different plasma conditions where the δB_{POL} measurements for the different (6x Mirnov, 3x LTCC-3D) sensors are taken.

6. Conclusions: lesson learnt for ITER

The development of LTCC magnetic sensors at the EPFL has started in 2007 in the framework of prototyping work for ITER, and the currently ongoing procurement of 290 LTCC-1D sensors for actual installation on ITER in many ways represents the culmination of this project. We can clearly draw a number of lessons from our work that we hope could be beneficial for ITER.

Table1. Measured vs. predicted electrical properties for the LTCC-1D modules used for the assembly of the 3D sensors. The predicted values are obtained with a racetrack model for the winding pattern. The ± shows the variability over all the functional LTCC-1D modules (331) actually used for the assembly of the LTCC-3D sensors.

	$R_{SELF}[\Omega]$	$L_{SELF}[\mu H]$	$NA_{EFF}[cm^2]$
measured	12.46±0.48	12.52±0.14	29.30±0.32
predicted	12.60	13.00	30.00

First, the main electrical characteristics of the LTCC sensors (NA_{EFF}, L_{SELF}, R_{SELF}, L_{MUT} and NA_{PAR} for multi-D assemblies) can be quite accurately predicted using the appropriate circuit modelling, even for very complex LTCC-3D sensors (see fig7, table1 and table2), but this requires non-trivial mathematics involving, for instance, the calculation of the so-called solenoid filling factor [18] and of partial inductances and distributed capacitances.

Table2. Measured vs. predicted electrical properties for the δB_{RAD} measurement in the LTCC-3D sensors. The predicted values are obtained using a concentric model for the winding pattern. The ± shows the variability over all the functional modules (18).

	measured	predicted
$R_{SELF}[\Omega]$	18.23±0.41	18.20
$L_{SELF}[\mu H]$	7.79±0.10	7.60
$NA_{EFF}[cm^2]$	216.18±1.80	215.00
$L_{MUT}[\mu H]$	0.62±0.17	0.85
$NA_{PAR,zx}[cm^2]$	2.48±0.35	2.65
$NA_{PAR,zy}[cm^2]$	2.71±0.45	3.02

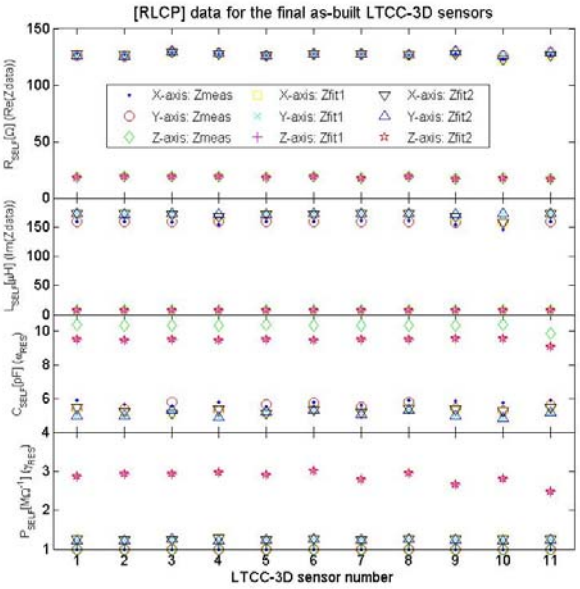

Fig7. Measured vs. predicted electrical properties for the 11x fully assembled LTCC-3D sensors. The measurements (labelled Z_{MEAS}) are obtained from the impedance data, while the two fits ($Z_{FIT1,2}$) come from different rational functions used to model the impedance measurements.

Second, we have achieved excellent manufacturing yields, comparable to the best industrial standards. As an example, for the LTCC-3D sensors we had a 100% yield for the alumina modules (18/18) and a 97.25% yield for the LTCC-1D modules (354/364, including two variants).

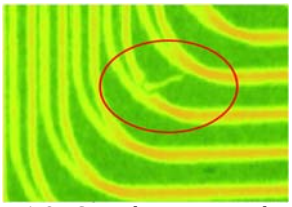

Fig8a. Some dust got trapped between the windings, shorting the electrical connection.

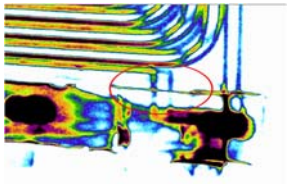

Fig8b. Incomplete filling of the vias, breaking the electrical continuity between layers.

This was obtained only after carefully revisiting each individual step of the actual manufacturing process, including the clean-ness of our clean room, which was indirectly evaluated using 3D X-rays tomography of as-built defective sensors to identify exactly the location and source of the defect (see fig8 for two examples). As a result of these analysis, a solution has also been found to recover partially defective sensors by adding sacrificial external windings (see fig9).

The main problem with the LTCC technology is that the sensor winding and the in-vessel cabling are now separate and of different materials. Different solutions have been successfully tested, all of them being rather cumbersome (see fig10), and indeed for ITER a very complex support and connection platform is envisaged to tackle this problem [11].

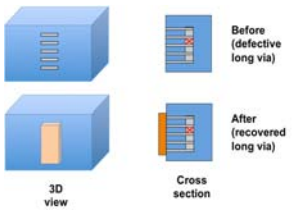

Fig9. Sacrificial external windings used to recover partially defective modules.

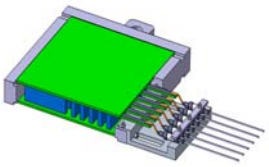

Fig10. The solution which has been implemented to connect the sensor and in-vessel wires.

Another perceived problem has always been that of a risk of transmutation of the conductive inks under the neutron and radiation fluxes expected in ITER (Ag→Cd, Au→Hg→Pb). This has been determined not to be an actual problem following irradiation tests of some pre-production samples [19], and more recently of the ITER LTCC-1D prototypes manufactured by EPFL [11].

Acknowledgments

This work has been carried out within the framework of the EUROfusion Consortium and has received funding from the Euratom research and training programme 2014-2018 under grant agreement No 633053. The views and opinions expressed herein do not necessarily reflect those of the European Commission. This work was also partly supported by the Swiss National Science Foundation.

References

[1] Y.Imanaka, Springer, 2004-12-10, ISBN 0-387-23130-7.
[2] H.Takahashi et al., RSI **72** (2001), 3249.
[3] D.Testa et al., SOFE 2009, 10.1109/fusion2009.5226525.
[4] G.Chitarin et al., FED **84** (2009), 593.
[5] D.Testa et al., SOFE 2009, 10.1109/fusion.2009.5226481.
[6] D.Testa et al., SOFT 2010; 10.1016/j.fusengdes.2011.03.118.
[7] M.Toussaint et al., SOFT 2010; 10.1016/j.fusengdes.2011.03.080.
[8] D.Testa et al., FST **59** (2011), 376; http://epubs.ans.org/?a=11653.
[9] D.Testa et al., SOFT 2014; 10.1016/j.fusengdes.2015.05.065.
[10] S.Peruzzo et al., TPS **44** (2016), 1704; 10.1109/TPS.2016.2580380.
[11] Private communication from personnel from F4E and ITER.
[12] A.Karpushov et al., SOFT 2016; 10.1016/j.fusengdes.2017.02.076.
[13] D.Testa et al., *Manufacturing, Installation, Commissioning and First Results with LTCC-3D High-Frequency Magnetic Sensors on TCV*, to be submitted to RSI, 2019.
[14] J.M.Moret et al., RSI 69 (1998), 2333.
[15] W.Heidbrink et al., PoF-B **5** (1993), 2176.
[16] L.Stipani, *Fishbones and de-trapping of fast ions during NBH discharges on TCV*, 15th IAEA TCM on Energetic Particles, 2017; poster contribution available in .pdf format by request to the corresponding author (duccio.testa@epfl.ch)
[17] J.P.Graves et al., Theory of Fusion Plasma Conference, 2018.
[18] A.E.Ruehli, IBM Journal of Research and Development, 1972, 470.
[19] L.Vermeeren et al., EPJ Web of Conferences **170**, 02008 (2018); https://doi.org/10.1051/epjconf/201817002008.